Hofstadter moiré butterfly in twisted trilayer graphene

Muhammad Imran [1], Paul M. Haney,[2] and Yafis Barlas [1]
[1]*Department of Physics, University of Nevada, Reno, Nevada 89557, USA*
[2]*Physical Measurement Laboratory, National Institute of Standards and Technology, Gaithersburg, Maryland 20899, USA*

(Received 10 December 2022; revised 8 June 2023; accepted 24 July 2023; published 10 August 2023)

Mirror-symmetric twisted trilayer graphene (tTLG) is composed of even-parity twisted bilayer graphene (tBLG)-like bands and odd-parity Dirac-like bands. Here, we study the mirror-symmetric and mirror-asymmetric Hofstadter moiré (HM) fractal bands of tTLG. A quantum parity Hall state is identified in mirror-symmetric tTLG at experimentally accessible charge densities. This mirror-symmetry-protected topological phase exhibits simultaneous quantized Hall and longitudinal resistances. The effects of the displacement field on the HM fractal bands of tTLG and topological phase transitions are also studied. The application of an electric displacement field results in an emergent weakly dispersive band at the charge neutrality point for a range of twist angles. This zero-energy state resides in the middle layer. It is isolated from the HM spectrum by an energy gap that scales proportional to the applied displacement field, making it a prime candidate to host correlated topological states.

DOI: 10.1103/PhysRevB.108.085417

I. INTRODUCTION

Moiré superlattices possess a periodicity much larger than the underlying crystal lattice spacing and for this reason provide an ideal test bed for investigation of the various topological phases of Hofstadter moiré fractal patterns [1–7]. These fractals are significantly influenced by twist angles and substrate interactions [2–4]. More importantly, electron-electron interactions in the Hofstadter moiré bands can result in correlated [8] and exotic topological phases [9]. Such "twistronic" engineering of flat bands in twisted 2D crystals is a promising route to discover novel interaction-driven correlated and topological phases [10–25]. A recently discovered class of these systems is alternating twist multilayer graphene. These systems consist of $m \geqslant 3$ graphene monolayers with a twist angle (θ) that alternates between $+\theta$ and $-\theta$ between each successive pair of layers [26–32]. In alternating twisted multilayer graphene, electric fields perpendicular to the sample, in addition to twist angles and substrate interactions, can significantly modify the Hofstadter moiré fractal patterns. This tunability of the Hofstadter moiré fractals can result in emergent regimes that might be ideal for realizing novel correlated and topological phases [8,9,24,25].

In this paper, we report on the topological properties and energy bands of Hofstadter moiré fractals in twisted trilayer graphene (tTLG). Without a displacement field, tTLG obeys mirror symmetry [33–36]. This allows for decomposition into tBLG-like even-parity bands and monolayer graphene (MLG)-like Dirac odd-parity bands [26,27,32]. At high magnetic fields, this results in the coexistence of a tBLG-like Hofstadter moiré pattern with an MLG-like Landau level (LL) spectra in mirror-symmetric tTLG. The resultant even-parity tTLG Hofstadter moiré patterns at zero displacement field are consistent with earlier studies of the Hofstadter moiré patterns in tBLG [2–4]. However, the tTLG Hofstadter moiré patterns exhibit a different sequence of Chern numbers due to the simultaneous presence of the odd-parity MLG-like LLs.

More importantly, the mirror symmetry stabilizes a symmetry-protected topological phase, which we call the quantum parity Hall state. It originates from counterpropagating branches of even- and odd-parity edge states with different numbers of branches and opposite signs of the Hall conductivity in each parity sector. This state is present in the angle regimes $\theta \approx 1.6^\circ$ to 2.5° at accessible charge densities in tTLG. Since mirror symmetry forbids backscattering between different parity sectors, this state *exhibits simultaneous quantization of the Hall and longitudinal resistances*. Similar quantum Hall parity states have been identified in ABA-stacked trilayer graphene at neutral charge density [36,37].

In a displacement field, the Hofstadter moiré pattern is significantly modified due to the hybridization of the tBLG-like band with the MLG-like Landau levels (LLs). The system exhibits a fractured Hofstadter moiré butterfly pattern, followed by an emergent zero-energy weakly dispersive band. This weakly dispersing flat band is pinned to the charge neutrality point and separated from the rest of the spectrum by a band gap. In the angle regime $\theta \approx 1.7^\circ$ to 2.5°, the band gap increases linearly with the applied displacement field energy $\Delta_\perp$. This is accompanied by a slight increase in the bandwidth for the range $\Delta_\perp = 5$ meV to 30 meV. This zero-energy band resides primarily in the middle layer. Its energetic and topological properties can be tuned by the applied displacement field, making it a promising candidate for hosting many-body interacting ground states [9].

The paper is organized as follows. In Sec. II, we discuss the mirror-symmetric Hofstadter moiré butterfly, its band dispersion, and topological properties as a function of twist angles. Section III studies the origin and properties of the emergent zero-energy weakly dispersive band induced by electric fields in tTLG. Finally, in Sec. IV, we discuss the relevance of our results to experiments on tTLG at high magnetic fields. The details of the calculations, model Hamiltonian of tTLG, and methods are relegated to the Appendixes.

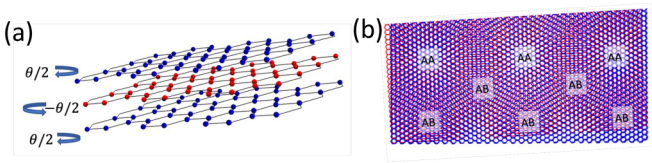

FIG. 1. (a) Lattice structure of twisted trilayer graphene with the top and bottom layer rotated by $\theta/2$ while the middle layer is rotated by $-\theta/2$. (b) Moiré pattern in twisted trilayer graphene with local AA and AB stacking regions.

II. MIRROR-SYMMETRIC tTLG HOFSTADTER MOIRÉ BUTTERFLY

The lattice structure of the tTLG lattice exhibits mirror symmetry about the middle layer, as indicated in Fig. 1(a). This facilitates a description of energy bands in terms of parity eigenstates [32,34,35]. We denote sublattice $A(B)$ on layer i with $A_i(B_i)$. The even-parity orbital combinations are then given by (A_+, B_+, A_2, B_2) while the odd-parity orbitals are (A_-, B_-), where $A_\pm = (A_1 \pm A_3)/\sqrt{2}$ and $B_\pm = (B_1 \pm B_3)/\sqrt{2}$. We take the relative in-plane displacement $d = 0$ and denote the top (bottom) layers angle $\theta/2$ while the middle layer angle $-\theta/2$. The band dispersion due to the moiré pattern formed at small twist angles can be captured by extensions of the Bistritzer-MacDonald (BM) Hamiltonian [10]. The BM model captures the effect of the periodic tunneling between the layers in the AA and AB stacked regions [see Fig. 1(b)], denoted by $w_{AB} = w = 97.5\,\text{meV}$ and $w_{AA} = \eta w$ with $\eta = 0.82$, respectively (see Appendix A for the tTLG Hamiltonian). At zero displacement fields, due to mirror symmetry, the Hamiltonian can be decomposed into tBLG-like Hamiltonian with enhanced tunneling parameter $w \to \sqrt{2}w$ and an MLG-like Dirac band [27,32].

The large moiré periodicity of twisted 2D crystal results in a fractal Hofstadter moiré (HM) bands at high magnetic fields. We used the parity eigenstate basis to calculate the HM bands of tTLG with the gauge choice $\mathbf{A} = B(-y, 0)$. The Hamiltonian was expressed in the basis set $\{|n, Y_i, \alpha, \sigma\rangle\}$, where n denotes the Landau level (LL) index at the guiding center positioned at Y_i (which corresponds to a lattice site in the unit cell) on the sublattice α. The index $\sigma = 1, 2, 3$ denotes the parity eigenspinors with the assignments $1 = (A_+, B_+)$, $2 = (A_2, B_2)$, and $3 = (A_-, B_-)$. The details of the calculation are presented in Appendix A.

Our calculations for tTLG exhibited rich structures in the HM spectrum, which can be tuned by the electric field and twist angles. Figure 2 shows the HM butterfly for mirror-symmetric tTLG at three representative angles ($\theta = 2^\circ$, 1.6°, and 1.5°). The Hall conductivity, in units of e^2/h, is shown in the spectral gaps. In Fig. 2, the even-parity bands are depicted in blue or black, while the odd-parity bands are shown in red. The Landau bands originating from the odd-parity sector can be distinguished by $\epsilon_n \propto \sqrt{B}$, while the energy of the even-parity bands exhibit a tBLG HM fractal pattern. Similar HM butterfly patterns for tBLG have been reported in Ref. [3]. Our even-parity band HM butterfly patterns are consistent with these reports but now occur at twice the magnetic fields

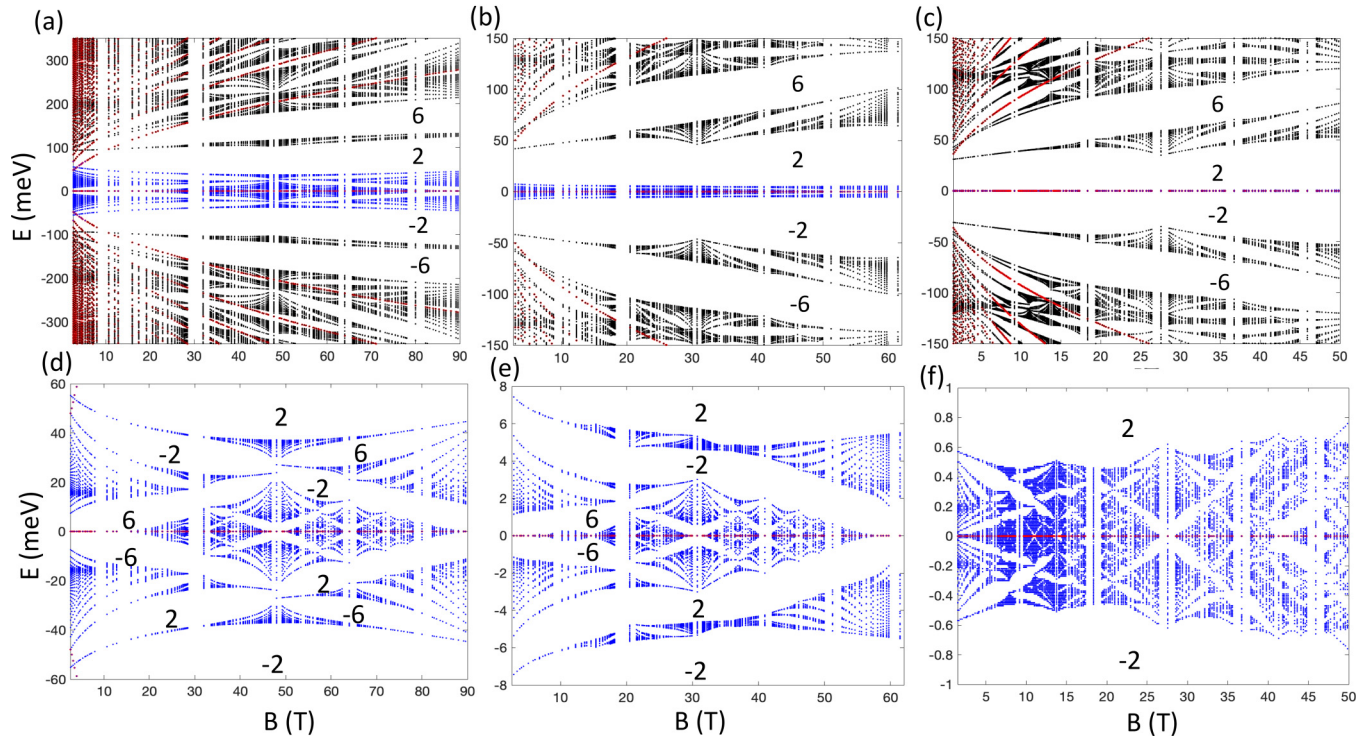

FIG. 2. Hofstadter moiré butterfly patterns in tTLG for zero displacement field. Energy eigenvalue dispersion as a function of the applied magnetic field at the angles (a) $\theta = 2^\circ$, (b) $\theta = 1.6^\circ$, and (c) $\theta = 1.51^\circ$(magic angle) with $w = 97.50\,\text{meV}$ and $\eta = 0.82$. In [(a)–(c)], the even-parity bands are denoted by black/blue, while the odd-parity bands are denoted by red. The values in the spectral gaps indicate the Hall conductivity σ_{xy} in units of e^2/h. For clarity, the details of the central band regions in [(a)–(c)] depicted in blue for even-parity bands and red for the odd-parity bands, are magnified in [(d)–(f)].

due to the $\sqrt{2}$ enhancement of the twist angle in the tTLG even-parity sector. The HM bands of tTLG exhibit unitary particle-hole symmetry [26,38] resulting in a symmetric spectrum with respect to the neutral charge density point (see Appendix A for a discussion of this symmetry).

We primarily focused on three angles, each indicative of three distinct regimes of the HM butterfly. A detailed version of these central bands of the HM butterfly is shown in Figs. 2(d)–2(f). The $\theta = 2^\circ$ HM butterfly is representative of the twist angle range $\theta \approx 1.7^\circ$ to 2.5°. In this regime, we found an emergent Hofstadter pattern similar to the Hofstadter pattern of the tight-binding model for graphene. This feature has been observed in previous studies [3], and this duality can be proved in the weak tunneling or high magnetic field limit, where LL mixing becomes negligible. This duality survives even in the presence of LL mixing for this angle regime, most likely associated with the underlying symmetries of the moiré lattice potential. A more detailed description of this duality will be provided elsewhere.

In contrast, for $\theta = 1.6^\circ$, we found a spectral gap for all magnetic fields. Similar results were obtained for the range of angles $\theta \approx 1.65^\circ$ to 1.55°, after which the pattern changed significantly. At the magic angle $\theta = 1.51^\circ$, the HM pattern is modified and bears no resemblance to the Hofstadter pattern in monolayer graphene. The bandwidth of the central bands decreases nearly an order of magnitude when compared to the HM pattern at $\theta = 2^\circ$. Below the magic angle at $\theta = 1.45^\circ$ another pattern reemerged similar to $\theta = 1.6^\circ$.

In Fig. 2, the integers in the spectral gaps of the HM butterflies denote the Hall conductivity, σ_H in units of e^2/h. The numerically attained eigenfunctions were employed with the Wilson loop procedure [39] to calculate the Chern numbers and Berry flux (see Appendix B for details of this method). We calculated the Hall conductivity within the larger spectral gaps $\gtrsim$5 meV. The Hall conductivity at the charge neutrality point $\sigma_H(\epsilon_F = 0) = 0$ was regularized to zero and included the spin and valley degeneracy. The Chern numbers and Hall conductivity of the emergent HM pattern for $\theta = 2^\circ$ in the even-parity sector of tTLG are the same as the monolayer graphene Hofstadter butterfly. This aspect of the duality for tBLG has been reported in Ref. [3]. However, in tTLG, the Hall conductivity is the sum of the Hall conductivity of tBLG even-parity HM bands and the MLG bands odd-parity LLs.

III. QUANTUM PARITY HALL EFFECT

A consequence of mirror symmetry in tTLG is a symmetry-protected topological (SPT) phase with simultaneous quantization of the longitudinal and Hall resistance. This mirror-SPT (mSPT) phase, which we call the quantum parity Hall phase was identified at neutral charge density in ABA trilayer graphene [36,37]. In tTLG, this state occurs at finite charge density. It is marked by unequal branches of counterpropagating even-parity and odd-parity edge modes associated with tBLG-like HM bands and MLG-like LL bands. In Figs. 3(a) and 3(b), we label the regions where the quantum parity Hall state appears by the number of edge states associated with each parity sector, blue(red) for even(odd) parity.

The Hall conductivity is positive(negative) for negative(positive) energies in these regions. Since the neutral

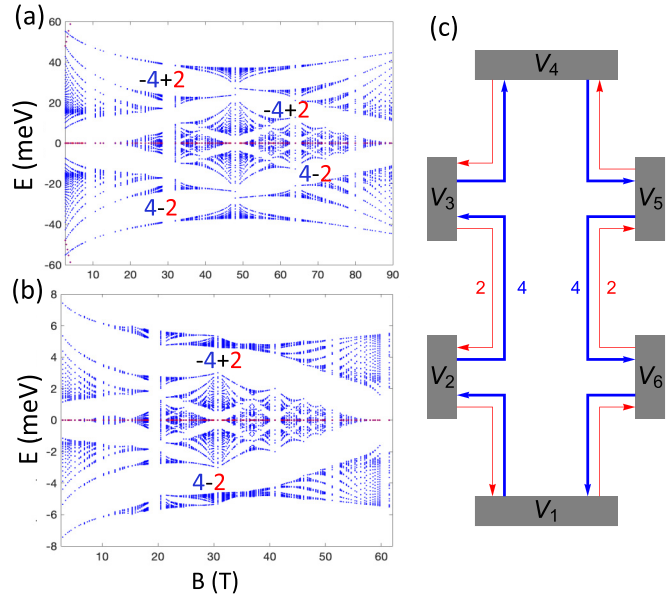

FIG. 3. Quantum parity Hall phase in the Hofstadter moiré butterfly patterns of tTLG for (a) $\theta = 2^\circ$ and (b) $\theta = 1.6^\circ$. The number of edge states associated with the even-parity tBLG-like bands are in blue, while the MLG-like bands are in red, in units of e^2/h. (c) Edge state schematic of the quantum parity Hall phase in a six-terminal Hall-bar geometry at positive charge densities.

charge density is defined at zero energy, this corresponds to a positive(negative) sign of Hall conductance for hole-like(electron-like) charge densities. This is an essential feature of this quantum Hall parity state in tTLG. From our calculations of Chern numbers, we only found one instance of this state. Still, other types of mSPT phases can be realized in regions with smaller spectral gaps $\lesssim$5 meV. They can be identified by negative(positive) even-parity tBLG-bands Chern numbers at positive(negative) charge densities.

Figure 3(c) shows the edge states for the quantum parity Hall phase in a six-terminal Hall bar geometry for positive charge densities. Two edge modes originate from the odd-parity LL bands (shown in red), and four counterpropagating edge modes arise from the even-parity Hofstadter bands (shown in blue). Since the edge states in the mirror sectors have unequal branches of edge modes, they exhibit simultaneous quantized Hall and longitudinal resistances. The edge modes are protected from backscattering by mirror symmetry. The resistances in the Hall bar geometry can be calculated from the Landauer-Buttiker approach [40] (see Appendix C) for the quantum parity Hall state, giving

$$R_{14,26} = \frac{h}{6e^2}; \quad R_{14,32} = \frac{h}{9e^2}; \quad R_{14,14} = \frac{4h}{9e^2}, \tag{1}$$

where $R_{ij,kl}$ is defined as the ratio of the voltage to the current measured between the kth and the jth, with current applied from the ith to the jth lead. The edge states of the quantum parity Hall phase and their stability to disorder are discussed in what follows.

The effect of bulk and edge mirror asymmetry on the quantum parity Hall state can be estimated from general arguments. To observe the quantum parity Hall states, the bulk

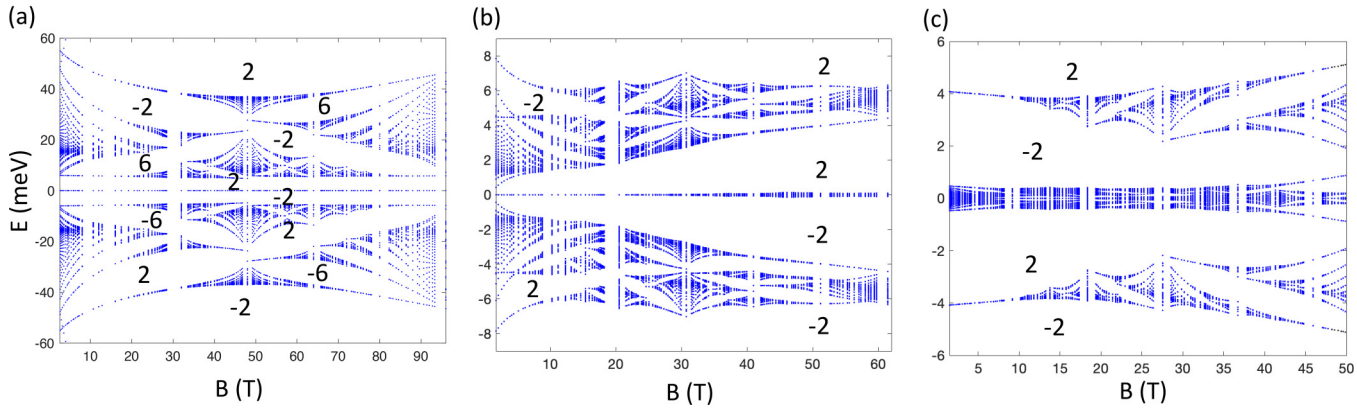

FIG. 4. Hofstadter moiré butterfly patterns in tTLG for an electric displacement field strength $\Delta_\perp = 10\,\text{meV}$ at the angles (a) $\theta = 2^\circ$, (b) $\theta = 1.6^\circ$, and (c) $\theta = 1.51^\circ$(magic angle) with $w = 97.50\,\text{meV}$ and $\eta = 0.82$. The values in the spectral gaps indicate the Hall conductivity σ_{xy} in units of e^2/h.

gap Δ_{QPH} must be larger than the energy associated with mirror asymmetry in realistic samples. This energy scale is $\hbar v k_D \Delta\theta \sim 62.2\Delta\theta$ meV, where $\Delta\theta$ is the difference between the angle of the top and bottom layer. For the quantum parity Hall state at $\theta \sim 2^0$, we estimate that the bulk gap will survive for $\Delta\theta \leqslant 0.1^0$. This estimate decreases as the QPH band gap reduces when the twist angle approaches the magic angle.

To estimate the effect of edge asymmetry, we model the interparity channel mixing as disorder along a one-dimensional bosonic edge, which can be characterized by a localization length [41]. It determines the sample dimensions for which the quantum parity Hall state can be observed. If the distance between the leads in Fig. 3(c) is smaller than the localization length, the transport channel becomes ballistic, and the conductance will be given by Eq. (1). The calculation of the localization length and its dependence on the disorder strength will be provided elsewhere. Alternately, sharp local gates can be used to define an electrostatic edge inside the sample, thus preserving the requirement of mirror symmetry along these gate-defined edges.

IV. EMERGENT ZERO-ENERGY STATE IN tTLG

The displacement field breaks mirror symmetry, hybridizing the Dirac LLs with the even-parity HM bands of the tBLG-like even-parity sector. Figures 4(a)–4(c) show the HM pattern in the presence of a displacement field of strength $\Delta_\perp = 10$ meV. The most striking feature is the emergence of two spectral gaps adjacent to the charge neutrality point. For all three angle regimes, we observed this fractured fractal pattern in a displacement field when compared to the HM fractal patterns in Figs. 2(d)–2(f). This is accompanied by the emergence of a weakly dispersing zero-energy band pinned at the charge neutrality point. This zero-energy band disperses with a small bandwidth $\approx$0.1 to 0.4 meV for the twist angle $\theta = 2^\circ$. However, its bandwidth slightly increases at smaller twist angles as a function of the magnetic field. The spectral gap at zero-energy is given by $\approx\Delta_\perp/2$ for $\theta = 2^\circ$, and it is independent of the magnetic field within numerical accuracy. This spectral gap results from a level repulsion mechanism, as discussed below.

Another striking feature in a displacement field is a topological phase as a function of the twist angle. This is evident in the Hall conductivity at $\theta = 2^0, 1.6^0$ of the gapped state above the charge neutrality point which changes from $\sigma_{xy} = 2e^2/\hbar$ to $\sigma_{xy} = -2e^2/\hbar$ at $\theta = 1.51^0$. This is accompanied by a similar change in Hall conductivity below the charge neutrality point. This topological transition indicates a significant band reconstruction between the twist angles $\theta = 1.6^\circ$ and $\theta = 1.51^\circ$. These transitions are associated with the Berry curvature's tunability and band dispersion as a function of the electric field. This phase transition is evident in the corresponding Wannier plots for tTLG (see Appendix B).

The most striking feature is the emergence of a zero-energy flat band multiplet in the angle regimes $\theta = 1.7^\circ$ to 2.5° under a displacement field. This zero-energy flat band multiplet entirely resides in the middle layer and is q-fold degenerate, where $\phi = p/q$ is the inverse magnetic flux per unit cell. The emergent zero-energy state results from the level repulsion of the LL states in the top and bottom layers induced by the displacement field, which leaves an isolated state derived from the $N = 0$ LL in the A_2 orbital. Below we describe the origin of this state in more detail for the **K** valley. Key to this argument is the observation that the displacement field leads to level repulsion between A_- and A_+ states, which is much greater than the interlayer tunneling-induced modification of the A_2 LL energy. The argument for the other valley $\mathbf{K}'$ can be attained by interchanging the sublattices.

We first discuss the influence of interlayer tunneling on the $n = 0$ LLs on the A sublattice. We assume zero displacement field and consider the chiral limit ($\eta = 0$), corresponding to the absence of tunneling between the same orbitals (i.e., $w_{A_+A_2} = w_{B_+B_2} = 0$) in the even-parity tBLG-like bands [23]. In a magnetic field when $\eta = 0$, the $N = 0$ LL in valley **K** lies on the sublattice A_+, A_2 in the even-parity sector, and A_- in the odd-parity sector. Since the $N = 0$ LLs are localized on the A sublattice, there is no direct coupling between the $N = 0$ LLs, as indicated in Fig. 5(a). The $N \neq 0$ LL are perturbatively coupled to the $N = 0$ LL due to $w_{A_+B_2}$ and $w_{B_+A_2}$ tunneling. The effect of this tunneling can be captured by an effective coupling $\lambda_t \propto (w/(\hbar v k_\theta))\phi \exp(-2\pi\phi/\sqrt{3})$. In Fig. 5(a), this mixing is indicated by the dashed lines, where we only show the coupling in valley **K**.

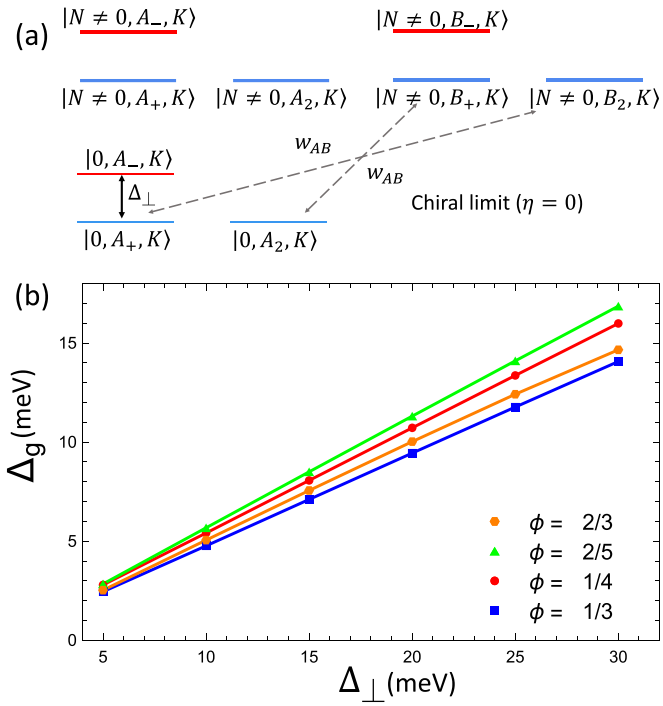

FIG. 5. (a) Schematic representation of the coupling in the chiral limit ($\eta = 0$) in valley **K** for the $N = 0$ with the $N \neq 0$ LLs. The direct coupling in $N = 0$ LL due to the displacement field is represented by the solid black line, while the perturbative coupling due to tunneling between the A and B sublattices is denoted by the dashed line. (b) Band gap as a function of the displacement field for different values of inverse flux per unit cell $\phi = p/q$, all energies are in meV. All results are for the twist angle $\theta = 2^\circ$.

We next consider the impact of the displacement field on LL energy levels. When a displacement field is applied, the A_+ orbital hybridizes with the A_- orbital in the odd-parity sector. This direct coupling is shown in the solid line in Fig. 5(a). These states gap out due to level repulsion with the energy separation scaling as $\lambda_\Delta \approx \Delta l_B/(\hbar v) \propto \sqrt{\phi}$. This level repulsion mechanism leaves behind the zero-energy state on the middle layer on the orbitals A_2 at zero energy. Therefore, in the chiral limit $\eta = 0$, the emergent zero-energy state in the HM pattern at $\theta = 2^\circ$ is localized in the middle layer on sublattice A_2 in the **K** valley. The zero-energy level has components $N \neq 0$ LL due to mixing induced by the $w_{A_+B_2}$ and $w_{A_2B_+}$ interlayer tunneling terms, as described in the previous paragraph. The ratio of the interlayer tunneling λ_t to the displacement field-induced coupling λ_Δ scales as $\sqrt{\phi}\exp(-\phi)$, which exhibits exponential suppression at low fields. This indicates that the level repulsion mechanism dominates for $B \lesssim 40\,\mathrm{T}$ and results in the localization of the zero-energy state on the middle layer.

In the chiral limit, the calculated projected weight of the emergent zero-energy state averaged over the BZ mesh on the $N = 0$ LL orbital in the middle layer was ≈80%, indicating some mixing with higher LL in the middle layer. This mixing can be characterized by λ_t and results in ≈20% mixing with $N \neq 0$ LL in the middle layer. While our arguments are valid for lower magnetic fields, they had to be numerically verified at higher values of the magnetic fields or smaller values of ϕ. Although we considered the chiral limit in our description above, we find that in both the chiral limit and for $\eta = 0.82$, the calculated projected weight of the zero-energy state on the middle layer was ≈1 and independent of the value of ϕ. The same results are obtained for various displacement fields. Furthermore, the calculated projected weight of the emergent zero-energy state averaged over the BZ-mesh on the $N = 0$ LL orbital in the middle layer was ≈60%, indicating significant mixing ≈40% with $N \neq 0$ LLs in the middle layer.

More evidence of the level repulsion mechanism can be inferred from the behavior of the energy gap above the zero-energy state Δ_g as a function of the displacement field. The energy gap $\Delta_g \approx \Delta_\perp/2$ grows linearly as a function of the displacement field [see Fig. 5(b)]. The bandwidth of the zero-energy state $\Delta_w \approx 0.1$ to 0.4 meV is much smaller than the band gap and varies slightly with the electric field. We also found that the Berry curvature deviation of the zero-energy state decreases as a function of the displacement field strength $\Delta_\perp$. This tunability of the Berry curvature and isolation of the emergent zero-energy state provide ideal conditions for realizing various interesting many-body interacting ground states [9]. Since the emergent zero-energy state has significant components of higher LL wavefunction, it is anticipated that the ground state at fractional filling will most likely be a Wigner crystal or charge density wave state [42–46]. Due to the complexity of the computational basis, these studies must be performed on lattice analogs of the HM pattern of tTLG.

V. CONCLUSIONS AND OUTLOOK

In conclusion, the displacement field provides an external knob to manipulate the topological phase and energy spectrum in the HM butterfly. The most striking is the emergence of a zero-energy state at the charge neutrality point within an accessible range of doping densities, whose separation from the energy spectrum can be tuned by the displacement field. The narrow bandwidth of the zero-energy band indicates the possibility of strongly correlated phases such as quantum Hall ferromagnetism [47–50], possible charge density waves [42–46], and fractional topological insulators [9,51–55]. Furthermore, the electric field can be used to access topological transitions. This makes it possible to probe the HM butterfly patterns in tTLG in transport or via scanning probe experiments.

In addition, we discovered a symmetry-protected topological phase for the mirror-symmetric case due to unequal counter-propagating edge modes exhibiting simultaneous Hall and longitudinal resistances. Interactions within each sector of the quantum parity Hall phase will most likely result in analogs of the exotic correlated quantum Hall phases detected in the ABA stacked trilayer graphene [36,37]. Interactions within the Hofstadter bands will also result in topological and correlated phases when the bandwidth is smaller than the interaction energy scale, which generally occurs for larger values of q. However, due to the nonmonotonic behavior as a function of the magnetic fields, as evidenced by the fractal nature of the HM butterfly patterns, the role of interactions requires detailed theoretical calculations for every value of ϕ, which is beyond the scope of this paper.

ACKNOWLEDGMENTS

M.I. and Y.B. acknowledge the support of UNR/VPRI Startup Grant PG19012. Y.B. acknowledges support from the Aspen Center for Physics, which is supported by NSF Grant No. PHY-1607611, where part of this work was performed.

APPENDIX A: tTLG HAMILTONIAN

The continuum Hamiltonian of the tTLG [10], which is valid for small angles, $\theta \approx 3^\circ$, can be expressed in terms of a six-component spinor, $\psi^\dagger_{\mathbf{K}} = (\phi^\dagger_{1,\mathbf{K}}, \phi^\dagger_{2,\mathbf{K}}, \phi^\dagger_{3,\mathbf{K}})$, at the Dirac point $\mathbf{K}_+$,

$$H = \begin{pmatrix} h_\theta + \Delta_1 & T(\mathbf{r}) & 0 \\ T^\dagger(\mathbf{r}) & h_{-\theta} + \Delta_2 & T^\dagger(\mathbf{r}) \\ 0 & T(\mathbf{r}) & h_\theta + \Delta_3 \end{pmatrix}, \tag{A1}$$

where $h_{\pm\theta} = D(\theta)[-\imath\hbar v(\xi\sigma_x\partial_x + \sigma_y\partial_y)]D^\dagger(\theta)$ denotes the Dirac Hamiltonian on the rotated Brillouin zone (BZ), with $D(\theta) = \exp(\imath\sigma_z\theta/2)$, σ_i denotes the Pauli matrix acting on the sublattice degree of freedom. $\xi = \pm 1$ denotes the Dirac points corresponding to different valleys at the BZ momentum $\mathbf{K}_\xi = 4\pi/3a(\xi, 0)$. The momentum space tunneling matrix elements $T(\mathbf{r}) = \sum_{n=1}^3 \hat{T}_n e^{\imath\mathbf{q}_n\cdot\mathbf{r}}$ can be expressed in terms the matrices $\hat{T}_n$ with

$$\hat{T}_n = w(\eta\hat{\mathbb{I}} + \cos((n-1)\phi_0))\hat{\sigma}_x + \sin((n-1)\phi_0)\hat{\sigma}_y) \tag{A2}$$

where $\phi_0 = 2\pi/3$, and the tunneling parameters are $w_{AB} = w = 97.5$ meV, $w_{AA} = \eta w$ with $\eta = 0.82$. The tunneling matrices are related by C_{3z} symmetry of the lattice via unitary operator $U_{3z}(\phi_0) = \exp(i\sigma_z\phi_0/2)$. The momentum transfer vectors associated to the honeycomb moiré lattice $\mathbf{q}_1 = k_\theta(0, -1)$, $\mathbf{q}_2 = k_\theta(\sqrt{3}/2, 1/2)$, $\mathbf{q}_3 = k_\theta(\sqrt{3}/2, -1/2)$, where $k_\theta = 4\pi/(3a_M)$ is the distance between the mini-Dirac points and $a_M = a_0/(2\sin(\theta/2))$ is the moiré lattice spacing with $a_0 = 0.246$ nm.

In the parity basis, the tTLG Hamiltonian becomes

$$H(w, \eta, \Delta_\pm) = \begin{pmatrix} h_\theta + \Delta_+ & \sqrt{2}T(\mathbf{r}) & \Delta_- \\ \sqrt{2}T^\dagger(\mathbf{r}) & h_{-\theta} + \Delta_2 & 0 \\ \Delta_- & 0 & h_\theta + \Delta_+ \end{pmatrix}, \tag{A3}$$

where $\Delta_\pm = (\Delta_1 \pm \Delta_3)/2$ and from now on we take $\Delta_2 = 0$. The above Hamiltonian in Eq. (A3) is expressed in terms of a six-component spinor basis $(A_+, B_+, A_2, B_2, A_-, B_-)$, where $A_\pm = (A_1 \pm A_3)/\sqrt{2}$ and $B_\pm = (B_1 \pm B_3)/\sqrt{2}$ have even (+) and odd (−) parity with respect to this mirror symmetry, while the middle layer, A_2 and B_2 orbitals have even (+) parity.

For all our calculations, we make the zero-angle approximation, which corresponds to the choice $D(\theta) \sim \mathbb{I}$ valid for small angles $\theta \lesssim 5^0$. This gives $h_{\pm\theta} = -\imath\hbar v(\xi\sigma_x\partial_x + \sigma_y\partial_y)$, with a small (1%) change in the accuracy of the energy eigenvalues for small angles. The Hamiltonian in Eq. (A3) exhibits a unitary particle-hole symmetry. This unitary particle-hole symmetry Γ_{PH} is generated by $\imath\tau_y \otimes \mathbb{I}$, where τ_y acts on the even-parity tBLG component of the Hamiltonian. This unitary particle-hole symmetry can be expressed as $\Gamma_{PH}H(\mathbf{r})\Gamma^{-1}_{PH} = -H(-\mathbf{r})$. This unitary particle-hole symmetry must be distinguished from the chiral symmetry at $\eta = 0$. This chiral symmetry is expressed as $\Gamma_C H\Gamma_C^{-1} = -H$, where $\Gamma_C = \otimes_{i=1}^3\sigma_z$ and σ_z acts on the sublattice degrees of freedom in each layer. We refer the reader to Ref. [38] for a complete discussion of the discrete symmetries of tBLG.

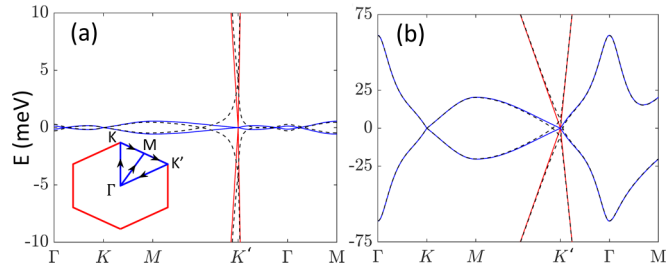

FIG. 6. Mirror-symmetric bands of tTLG at the magic angle (a) $\theta = 1.51^\circ$ and (b) $\theta = 2^\circ$ with even-parity tBLG-like bands in blue and the monolayer Dirac-like bands in red at $\Delta_- = 0$. The dashed line corresponds to the same angles with mirror symmetry broken ($\Delta_- = 10$ meV) by the presence of the electric field.

Due to the enhanced tunneling in the tBLG-like sector, the first magic angle occurs at $\theta_M = 1.51^\circ = 1.05^\circ\sqrt{2}$ with a bandwidth ≈0.5 meV. Figures 6(a) and 6(b) show the energy bands of tTLG at the first magic angle $\theta = 1.51^\circ$ and $\theta = 2^\circ$. In Figs. 6(a) and 6(b), the even-parity energy bands are plotted in blue, and the odd-parity energy bands are plotted in red. The odd-parity band exhibits a Dirac-like dispersion, while the even-parity bands exhibit the energy dispersion of tBLG. When the mirror symmetry is broken, for instance, by applying a displacement field $\Delta_\perp = 10$ meV the even- and odd-parity bands hybridize, as indicated by the black dashed line in Figs. 6(a) and 6(b).

To calculate the HM-bands of tTLG, we worked in the parity eigenstate basis, and the Landau gauge $\mathbf{A} = B(-y, 0)$ with the basis choice $\{|n, Y_i, \alpha, \sigma\rangle\}$, where n denotes the Landau level (LL) index at the guiding center positioned at Y_i (which corresponds to a lattice site in the unit cell) on the sublattice α. The index $\sigma = 1, 2, 3$ denotes the even(odd)-parity eigenspinors with the assignments $1 = (A_+, B_+)$, $2 = (A_2, B_2)$, and $3 = (A_-, B_-)$.

The moiré hopping pattern determines the Hamiltonian periodicity as opposed to the moiré unit cell [2]. The moiré hopping pattern has a larger periodicity, exactly six times the periodicity of the moiré unit cell $A_{Mh} = 3\sqrt{3}a_M^2$ [2], where $a_M \approxeq a_0/\theta$ for small angles with $a_0 = 0.246$ nm. The HM bands are calculated for rational values of flux per unit cell; with our choice of the unit cell, the inverse flux per unit cell is given by $\phi = 2\pi l_B^2/(3\sqrt{3}a_M^2) = p/q$, where p and q are coprimes. The magnetic field is $B = 4B_0\theta^2/\phi$, where $B_0 = 1$ T and θ is expressed in degrees.

The matrix elements in the basis set can be calculated from the Hamiltonian H. The matrix element associated to the diagonal Hamiltonian defined as $H_0 = H(0, 0, 0)$ are given by

$$\langle n, Y_i, A, \sigma|H_0|m, Y_j, B, \sigma'\rangle = \epsilon_0\sqrt{n}\delta_{n,m+1}\delta_{ij}\delta_{\sigma\sigma'}, \tag{A4}$$

where $\epsilon_0 = \sqrt{2}\hbar v/l_B$. It is important to point out that since the nth LL on sublattice A couples to the $(n+1)$th LL on sublattice B, for a finite LL cutoff N, the Nth LL on sublattice A shows up at zero energy, due to numerical truncation of the Hilbert space. To circumvent this issue, we used an asymmetric cutoff in our calculations and included the LL

orbitals, $n = 0, \ldots, N-1$ on sublattice A and $n = 0, \ldots, N$ on sublattice B. Of course, the situation is reversed in the other valley, and the Hamiltonian is just the transpose of the Hamiltonian in the valley **K**.

The tunneling matrix elements are only nonzero for LL wavefunctions between the spinors $\sigma = 1, 2$. Furthermore, due to the spatial dependence of the tunneling matrix elements different guiding centers Y_j are coupled with different σ indices. The tunneling matrix elements $T(\mathbf{r})$ in the LL basis can then be expressed as

$$\begin{aligned} T(\mathbf{r}) = \sum_{j,\mathbf{k}} \sum_{n,m} [&\hat{T}_{1;\alpha,\beta} \Gamma_{1;nm}(j,\mathbf{k}) |n, Y_j, \alpha, 1\rangle\langle m, Y_j, \beta, 2| \\ &+ \hat{T}_{2;\alpha\beta} \Gamma_{2;nm}(j,\mathbf{k}) |n, Y_j, \alpha, 1\rangle\langle m, Y_{j+1}, \beta, 2| \\ &+ \hat{T}_{3;\alpha\beta} \Gamma_{3;nm}(j,\mathbf{k}) |n, Y_j, \alpha, 1\rangle\langle m, Y_{j-1}, \beta, 2|], \end{aligned} \tag{A5}$$

where

$$\Gamma_{1;nm}(j,\mathbf{k}) = F_{nm}\left(\frac{\mathbf{q}_1 l_B}{\sqrt{2}}\right) e^{-\frac{4\pi\imath p}{q} j - \imath \frac{2}{\sqrt{3}} k_1}, \tag{A6}$$

$$\Gamma_{2;nm}(j,\mathbf{k}) = F_{nm}\left(\frac{\mathbf{q}_2 l_B}{\sqrt{2}}\right) e^{\frac{\pi\imath p}{q}(2j+1) + \frac{\imath}{\sqrt{3}} k_1 + \imath k_2}, \tag{A7}$$

$$\Gamma_{2;nm}(j,\mathbf{k}) = F_{nm}\left(\frac{\mathbf{q}_3 l_B}{\sqrt{2}}\right) e^{\frac{\pi\imath p}{q}(2j-1) + \frac{\imath}{\sqrt{3}} k_1 - \imath k_2}, \tag{A8}$$

where $\mathbf{k} = (k_1, k_2)$ is defined in units of $\Delta = (\sqrt{3}/2) k_\theta l_B^2 = 3(p/q) a_M$. With this parametrization, the magnetic BZ (mBZ) is given by $k_1 \in [0, 6\pi/(\sqrt{3}\phi))$ and $k_2 \in [0, 2\pi/q)$ in units of $\Delta = 3(p/q) a_M$.

The LL form factors $F_{n,n'}(x)$ are given by

$$F_{n,n'}(\mathbf{z}) = \begin{cases} \sqrt{\frac{n'!}{n!}} (\imath z^\star)^{n-n'} L_{n'}^{n-n'}(z^2) e^{-z^2/2} & n \geqslant n', \\ \sqrt{\frac{n!}{n'!}} (\imath z)^{n'-n} L_{n}^{n'-n}(z^2) e^{-z^2/2} & n' > n, \end{cases} \tag{A9}$$

where $z = z_x + \imath z_y$ with $z^2 = z_x^2 + z_y^2$ and $L_{n'}^{n-n'}$ are the associated Laguerre polynomials. The scaling of the tunneling matrix elements is primarily determined by the exponential factor $\exp(-(k_\theta l_B)^2/4) \sim \exp(-2\pi\phi/\sqrt{3})$, where ϕ is the inverse flux per unit cell. The diagonal factors scales as $F_{nn} \propto \sqrt{\phi} \exp(-2\pi\phi/\sqrt{3})$, whereas the off-diagonal factors obey $F_{nm} \propto \phi^{(|n-m|)/2} \exp(-2\pi\phi/\sqrt{3})$. Even though LL mixing is suppressed at low magnetic fields (or equivalently at higher values of ϕ), the LL spacing also reduces as $1/\sqrt{\phi}$. Therefore, several LLs must be included to achieve convergence.

To achieve convergence, our LL cutoff was determined by $N = 20(\max(w, \hbar v k_\theta)/\epsilon_0)^2$, where $\epsilon_0 = \sqrt{2}\hbar v/l_B$ with $\hbar v \approx 596$ meV nm. The dimension of the matrix for tTLG graphene for a given value of ϕ per valley is $N_{\text{dim}} = 6q(N + 1/2)$. The tTLG Hamiltonian was diagonalized over a 10×10 discrete mBZ mesh to calculate topological properties and a smaller mesh to generate the HM butterfly patterns.

APPENDIX B: TOPOLOGICAL PROPERTIES OF tTLG HM BUTTERFLY

Here, we review our procedure for calculating the topological properties. The Bloch function for the λ_ith HM bands in tTLG can be expressed as

$$\begin{aligned} u_{\lambda_i}(\mathbf{k}) = &\sum_{m=1,n}^{q,N} g_{\lambda_i,n,m}(\mathbf{k}) \sum_l \phi_n\big(x - k_2 l_B^2 - \Delta(m + lq)\big) \\ &\times \exp\left(\imath \frac{\Delta y}{l_B^2}(m + lq)\right) \\ &\times \exp\left(-\imath k_1 (x - \Delta m - q\Delta l)\right), \end{aligned} \tag{B1}$$

where ϕ_n corresponds to the Harmonic oscillator wavefunction and $g_{\lambda_i,m,n}(\mathbf{k})$'s are obtained numerically. The Chern number of the bands is calculated using the lattice gauge theory method introduced in Ref. [39]. For the case of Eq. (B1), there are two contributions to the Chern number, one associated with the lattice eigenvectors $g_{\lambda_i,m,n}(\mathbf{k})$, the lattice Chern number $\tilde{C}_\lambda$. In contrast, the other is associated with the band-folded LL wavefunctions ϕ_n.

The lattice Chern number for M-band multiplet with collection of bands with indices $\lambda_M = (\lambda_1, \lambda_2, \ldots, \lambda_M)$ and M-mulitple Bloch wavefunctions $(u_{\lambda_1}, u_{\lambda_2}, \ldots, u_{\lambda_M})$ we calculated the Bloch band Chern number $\tilde{C}_{\lambda_M}$ of the multiplet,

$$\tilde{C}_\lambda = \frac{1}{2\pi\imath} \sum_{\mathbf{k}_i} \prod_{\square} \det\left[\frac{G_{\lambda_M}(\mathbf{k}_i) G_{\lambda_M}(\mathbf{k}_i + \hat{\mu})}{\det\left|G_{\lambda_M}(\mathbf{k}_i) G_{\lambda_M}(\mathbf{k}_i + \hat{\mu})\right|}\right], \tag{B2}$$

where $G_{\lambda_M}(\mathbf{k}_i) = (g_{\lambda_1}(\mathbf{k}_i), g_{\lambda_2}(\mathbf{k}_i), \ldots, g_{\lambda_1}(\mathbf{k}_M))$ is the $N_d \times M$ matrix composed of the amplitude of the Bloch band wavefunction. Since our basis set comprises LLs, each band folded LL contributes to the Chern number by $1/q$. The total Chern number is the sum of the lattice Chern number and LL contribution associated with the multiplet,

$$C_\lambda = \tilde{C}_\lambda + \frac{M}{q}. \tag{B3}$$

The total Chern number C_λ is always an integer.

APPENDIX C: WANNIER DIAGRAMS

Figures 7(a) and 7(b) show the Wannier plots in the absence of any displacement field, where mirror symmetry is exact, for $\theta = 2^\circ$and $\theta = 1.51^\circ$, respectively. The slope of the straight lines corresponds to the Hall conductivity as indicated by Streda's formula $\bar{n} = \sigma\bar{\phi} + c$, where $\bar{n} = n/n_0$ refers to the normalized number density (n_0 is the total density that includes the spin and valley degeneracy), $\bar{\phi}$ refers to the tight binding alpha $\bar{\phi} = 1/(6\phi)$, σ denotes the Hall conductivity, and c denotes the intercept. The blue lines guide the eye and indicate Streda's formula applied to the HM pattern of tTLG. The high density of states in the wedge-shaped region in Figs. 7(a) and 7(b) is due to the simultaneous presence of the odd-parity zeroth LL.

Figures 7(c) and 7(d) show the Wannier plots for $\Delta_\perp = 10$ meV for $\theta = 2^\circ$and $\theta = 1.51^\circ$, respectively. The wedge shape region at charge neutrality has reduced intensity, indicating a gap opening in the presence of a displacement field. Additionally, the odd-parity Landau bands become weakly dispersive due to mixing with the even-parity tBLG energy bands. A displacement field can tune this topological transition; it can be identified in the Wannier plots as a

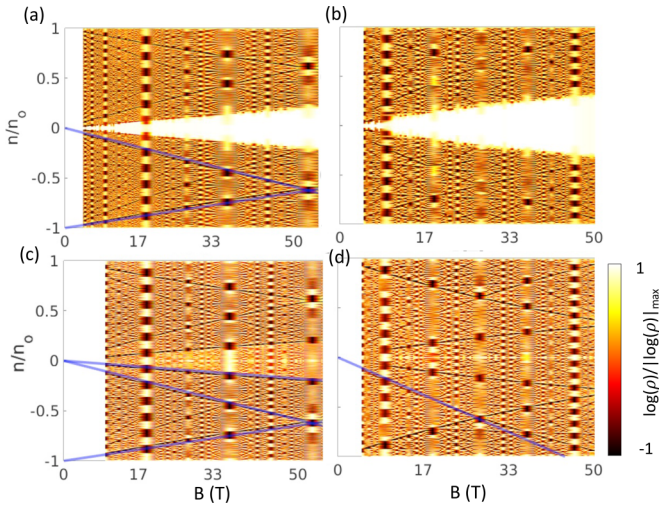

FIG. 7. Wannier plots for $\theta = 2^\circ$ [(a),(c)] and $\theta = 1.51^\circ$ [(b),(d)] with displacement field $\Delta_\perp = 0$, 10 meV. The straight blue lines are drawn from the Streda formula. We have only shown them for hole-HM bands. The sharp density of state features at the charge neutrality point is associated with the LL of odd-parity Dirac band of tTLG. As the gate voltage is applied, these sharp features in the density of states disappear due to mixing with Hofstadter energy bands. The absence of a white gap in the wedge-shaped region at the charge neutrality point indicates this.

more prominent downward sloping $-2(2)$ lines on the electron(hole) regions at the magic angle in Fig. 7(d).

APPENDIX D: LANDAUER-BUTTIKER THEORY

Consider a quantum parity Hall phase with m right-moving and n left-moving channels protected by mirror symmetry in a Hall bar geometry setup, as shown in Fig. 8. The current into the ith lead I_i can be expressed as

$$I_i = \frac{e^2}{h}\sum_j (T_{ij}V_j - T_{ji}V_i), \tag{D1}$$

where T_{ij} is the transmission probability of the current from the jth lead to the ith and V_i is the potential associated with the ith lead [40].

We assume perfect contacts, i.e., $T_{ij} = 1$, and that the current is applied to the first lead and drained from the fourth lead. The rest are floating contacts and act as voltage probes giving $I_2 = I_3 = I_5 = I_6 = 0$. We can write $I_1 = -I_4 = I$ because of the charge conservation. The voltages in terms of the current can be determined by solving the linear system of equations,

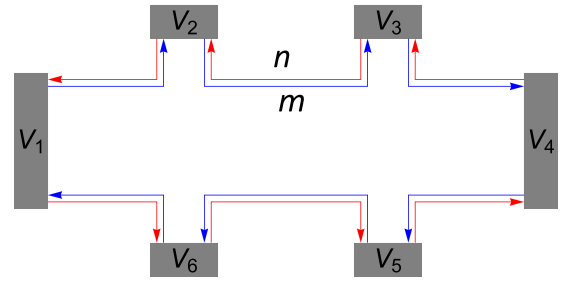

FIG. 8. Edge state schematic of the quantum parity Hall phase in a six-terminal Hall-bar geometry. The m right-moving electrons are indicated in blue, and the n left-moving electrons are shown in red.

$$V_1 = -\frac{h}{e^2}\left(\frac{n^2}{m^3+n^3}\right)I, \tag{D2}$$

$$V_2 = \frac{h}{e^2}\left(\frac{m-n}{m^2-mn+n^2}\right)I, \tag{D3}$$

$$V_3 = \frac{h}{e^2}\left(\frac{m^2+mn-n^2}{m^3+n^3}\right)I, \tag{D4}$$

$$V_4 = \frac{h}{e^2}\left(\frac{m}{m^2-mn+n^2}\right)I, \tag{D5}$$

$$V_5 = \frac{h}{e^2}\left(\frac{mn}{m^3+n^3}\right)I, \tag{D6}$$

with $V_6 = 0$. The resistance $R_{ij,kl}$ is defined as the ratio of the voltage to the current measured between the kth and the jth, with current applied from the ith to the jth lead gives

$$R_{14,26} = R_{14,35} = \frac{h}{e^2}\left(\frac{m-n}{m^2-mn+n^2}\right), \tag{D7}$$

while

$$R_{14,32} = R_{14,56} = \frac{h}{e^2}\left(\frac{mn}{m^3+n^3}\right), \tag{D8}$$

and

$$R_{14,41} = \frac{h}{e^2}\left(\frac{m^2+mn+n^2}{m^3+n^3}\right). \tag{D9}$$

[1] D. R. Hofstadter, Phys. Rev. B **14**, 2239 (1976).
[2] R. Bistritzer and A. H. MacDonald, Phys. Rev. B **84**, 035440 (2011).
[3] K. Hejazi, C. Liu, and L. Balents, Phys. Rev. B **100**, 035115 (2019).
[4] B. Lian, F. Xie, and B. A. Bernevig, Phys. Rev. B **102**, 041402(R) (2020).
[5] C. R. Dean, L. Wang, P. Maher, C. Forsythe, F. Ghahari, Y. Gao, J. Katoch, M. Ishigami, P. Moon, M. Koshino *et al.*, Nature (London) **497**, 598 (2013).
[6] D. J. Thouless, M. Kohmoto, M. P. Nightingale, and M. den Nijs, Phys. Rev. Lett. **49**, 405 (1982).
[7] J. A. Crosse, N. Nakatsuji, M. Koshino, and P. Moon, Phys. Rev. B **102**, 035421 (2020).
[8] Y. Saito, J. Ge, L. Rademaker, K. Watanabe, T. Taniguchi, D. A. Abanin, and A. F. Young, Nat. Phys. **17**, 478 (2021).
[9] Y. Xie, A. T. Pierce, J. M. Park, D. E. Parker, E. Khalaf, P. Ledwith, Y. Cao, S. H. Lee, S. Chen, P. R. Forrester *et al.*, Nature (London) **600**, 439 (2021).

[10] R. Bistritzer and A. H. MacDonald, Proc. Natl. Acad. Sci. USA **108**, 12233 (2011).

[11] Y. Cao, V. Fatemi, S. Fang, K. Watanabe, T. Taniguchi, E. Kaxiras, and P. Jarillo-Herrero, Nature (London) **556**, 43 (2018).

[12] M. Yankowitz, S. Chen, H. Polshyn, Y. Zhang, K. Watanabe, T. Taniguchi, D. Graf, A. F. Young, and C. R. Dean, Science **363**, 1059 (2019).

[13] Y. Cao, V. Fatemi, A. Demir, S. Fang, S. L. Tomarken, J. Y. Luo, J. D. Sanchez-Yamagishi, K. Watanabe, T. Taniguchi, E. Kaxiras *et al.*, Nature (London) **556**, 80 (2018).

[14] G. Chen, A. L. Sharpe, P. Gallagher, I. T. Rosen, E. J. Fox, L. Jiang, B. Lyu, H. Li, K. Watanabe, T. Taniguchi, J. Jung *et al.*, Nature (London) **572**, 215 (2019).

[15] X. Lu, P. Stepanov, W. Yang, M. Xie, M. A. Aamir, I. Das, C. Urgell, K. Watanabe, T. Taniguchi, G. Zhang *et al.*, Nature (London) **574**, 653 (2019).

[16] A. L. Sharpe, E. J. Fox, A. W. Barnard, J. Finney, K. Watanabe, T. Taniguchi, M. A. Kastner, and D. Goldhaber-Gordon, Science **365**, 605 (2019).

[17] C. Shen, Y. Chu, Q. Wu, N. Li, S. Wang, Y. Zhao, J. Tang, J. Liu, J. Tian, K. Watanabe *et al.*, Nat. Phys. **16**, 520 (2020).

[18] Y. Cao, D. Rodan-Legrain, O. Rubies-Bigorda, J. M. Park, K. Watanabe, T. Taniguchi, and P. Jarillo-Herrero, Nature (London) **583**, 215 (2020).

[19] X. Liu, Z. Hao, E. Khalaf, J. Y. Lee, Y. Ronen, H. Yoo, D. Haei Najafabadi, K. Watanabe, T. Taniguchi, A. Vishwanath, and P. Kim, Nature (London) **583**, 221 (2020).

[20] H. Polshyn, J. Zhu, M. A. Kumar, Y. Zhang, F. Yang, C. L. Tschirhart, M. Serlin, K. Watanabe, T. Taniguchi, A. H. MacDonald, and A. F. Young, Nature (London) **588**, 66 (2020).

[21] S. Chen, M. He, Y.-H. Zhang, V. Hsieh, Z. Fei, K. Watanabe, T. Taniguchi, D. H. Cobden, X. Xu, C. R. Dean, and M. Yankowitz, Nat. Phys. **17**, 374 (2021).

[22] P. San-Jose, J. González, and F. Guinea, Phys. Rev. Lett. **108**, 216802 (2012).

[23] G. Tarnopolsky, A. J. Kruchkov, and A. Vishwanath, Phys. Rev. Lett. **122**, 106405 (2019).

[24] I. Das, C. Shen, A. Jaoui, J. Herzog-Arbeitman, A. Chew, C.-W. Cho, K. Watanabe, T. Taniguchi, B. A. Piot, B. A. Bernevig, and D. K. Efetov, Phys. Rev. Lett. **128**, 217701 (2022).

[25] J. Herzog-Arbeitman, A. Chew, D. K. Efetov, and B. A. Bernevig, Phys. Rev. Lett. **129**, 076401 (2022).

[26] C. Mora, N. Regnault, and B. A. Bernevig, Phys. Rev. Lett. **123**, 026402 (2019).

[27] E. Khalaf, A. J. Kruchkov, G. Tarnopolsky, and A. Vishwanath, Phys. Rev. B **100**, 085109 (2019).

[28] T. Cea, N. R. Walet, and F. Guinea, Nano Lett. **19**, 8683 (2019).

[29] J. M. Park, Y. Cao, K. Watanabe, T. Taniguchi, and P. Jarillo-Herrero, Nature (London) **590**, 249 (2021).

[30] Y. Cao, J. M. Park, K. Watanabe, T. Taniguchi, and P. Jarillo-Herrero, Nature (London) **595**, 526 (2021).

[31] G. W. Burg, E. Khalaf, Y. Wang, K. Watanabe, T. Taniguchi, and E. Tutuc, Nat. Mater. **21**, 884 (2022).

[32] V. T. Phong, P. A. Pantaleón, T. Cea, and F. Guinea, Phys. Rev. B **104**, L121116 (2021).

[33] E. A. Henriksen, D. Nandi, and J. P. Eisenstein, Phys. Rev. X **2**, 011004 (2012).

[34] S. Latil and L. Henrard, Phys. Rev. Lett. **97**, 036803 (2006).

[35] M. Serbyn and D. A. Abanin, Phys. Rev. B **87**, 115422 (2013).

[36] Y. Barlas, Phys. Rev. Lett. **121**, 066602 (2018).

[37] P. Stepanov, Y. Barlas, S. Che, K. Myhro, G. Voigt, Z. Pi, K. Watanabe, T. Taniguchi, D. Smirnov, F. Zhang *et al.*, Proc. Natl. Acad. Sci. USA **116**, 10286 (2019).

[38] Z.-D. Song, B. Lian, N. Regnault, and B. A. Bernevig, Phys. Rev. B **103**, 205412 (2021).

[39] T. Fukui, Y. Hatsugai, and H. Suzuki, J. Phys. Soc. Jpn. **74**, 1674 (2005).

[40] M. Büttiker, Phys. Rev. B **38**, 9375 (1988).

[41] C. L. Kane and M. P. A. Fisher, in *Perspectives in Quantum Hall Effects*, edited by S. Das Sarma and A. Pinzuk (John Wiley, Hoboken, NJ, 1997), Chap. 4, pp. 109–157.

[42] A. A. Koulakov, M. M. Fogler, and B. I. Shklovskii, Phys. Rev. Lett. **76**, 499 (1996).

[43] M. M. Fogler, A. A. Koulakov, and B. I. Shklovskii, Phys. Rev. B **54**, 1853 (1996).

[44] M. M. Fogler and A. A. Koulakov, Phys. Rev. B **55**, 9326 (1997).

[45] M. P. Lilly, K. B. Cooper, J. P. Eisenstein, L. N. Pfeiffer, and K. W. West, Phys. Rev. Lett. **82**, 394 (1999).

[46] Y. Barlas, R. Côté, and M. Rondeau, Phys. Rev. Lett. **109**, 126804 (2012).

[47] K. Nomura and A. H. MacDonald, Phys. Rev. Lett. **96**, 256602 (2006).

[48] M. Kharitonov, Phys. Rev. Lett. **109**, 046803 (2012).

[49] P. Stepanov, Y. Barlas, T. Espiritu, S. Che, K. Watanabe, T. Taniguchi, D. Smirnov, and C. N. Lau, Phys. Rev. Lett. **117**, 076807 (2016).

[50] Y. Barlas, K. Yang, and A. H. MacDonald, Nanotechnology **23**, 052001 (2012).

[51] S. A. Parameswaran, R. Roy, and S. L. Sondhi, Phys. Rev. B **85**, 241308(R) (2012).

[52] N. Regnault and B. A. Bernevig, Phys. Rev. X **1**, 021014 (2011).

[53] B. Andrews and A. Soluyanov, Phys. Rev. B **101**, 235312 (2020).

[54] C. Repellin and T. Senthil, Phys. Rev. Res. **2**, 023238 (2020).

[55] P. J. Ledwith, G. Tarnopolsky, E. Khalaf, and A. Vishwanath, Phys. Rev. Res. **2**, 023237 (2020).